

A 400 G Ω Input-Impedance Active Electrode for Non-Contact Capacitively Coupled ECG Acquisition With Large Linear-Input-Range and High CM-Interference-Tolerance

Mingyi Chen ^{ID}, Member, IEEE, Ho Sung Chun, Member, IEEE, Iván Dario Castro ^{ID}, Tom Torfs ^{ID}, Quiyang Lin, Student Member, IEEE, Chris van Hoof, Member, IEEE, Guoxing Wang ^{ID}, Senior Member, IEEE, Yong Lian, Fellow, IEEE, and Nick van Helleputte ^{ID}, Member, IEEE

Abstract—Electrocardiogram (ECG) is one of the major physiological vital signs and an effective monitoring method for patients with cardiovascular diseases. However, existing ECG recordings require a galvanic body contact, which is unpractical in daily life. This paper presents the design of an ECG chip that facilitates non-contact ECG recording through capacitive coupling. With the input impedance boosting techniques, as well as an active driven-right-leg (DRL) which boosts common-mode rejection ratio to 70 dB, the single-ended capacitive feedback active electrode (AE) achieves ultra-high input impedance of 400 G Ω (< 0.5 Hz), a large common-mode interference tolerance (2.8 V_{PP}), and a high linear-input-range (220 mV_{PP}). Implemented in 0.18 μ m 5V CMOS process, the prototype occupies an area of 1.23 mm², and consumes 18 μ A and 13 μ A for the AE and DRL, respectively. Real life non-contact capacitively coupled ECG acquisition has been demonstrated, obtaining ECG waves and heart rate in the presence of motion artifacts as well as ambient interference.

Index Terms—Active electrode (AE), capacitively coupled, common-mode (CM) interference, electrocardiogram (ECG), linear-input-range, non-contact, ultra-high input impedance.

I. INTRODUCTION

CARDIOVASCULAR diseases (CVDs) are worldwide leading causes of deaths. 17.9 million people die each year from CVDs, an estimated 31% of all deaths worldwide [1]. The high cost of hospital-centered care and the high expenditure on treatments call for the transformation to low-cost, proactive, and

Manuscript received October 2, 2018; revised January 27, 2018 and January 16, 2019; accepted January 21, 2019. Date of publication January 28, 2019; date of current version March 22, 2019. This paper was recommended by Associate Editor B. Gosselin. (Corresponding author: Mingyi Chen.)

M. Chen is with IMEC, Heverlee 3001, Belgium, and also with the Shanghai Jiao Tong University, Shanghai 200240, China (e-mail: mingyi.chen@imec.be; mychen@sjtu.edu.cn).

H. S. Chun, I. D. Castro, T. Torfs, Q. Lin, C. van Hoof, and N. van Helleputte are with IMEC, Heverlee 3001, Belgium (e-mail: hosung.chun@imec.be; ivand.castro@imec.be; tom.torfs@imec.be; quiyang.lin@imec.be; chris.vanhoof@imec.be; nick.vanhelleputte@imec.be).

G. Wang and Y. Lian are with the Shanghai Jiao Tong University, Shanghai 200240, China (e-mail: guoxing@sjtu.edu.cn; elelian@sjtu.edu.cn).

Color versions of one or more of the figures in this paper are available online at <http://ieeexplore.ieee.org>.

Digital Object Identifier 10.1109/TBCAS.2019.2895660

outpatient-centered healthcare, with the ultimate goal to assist patients out of the hospital without disturbing their daily life.

As one of the major physiological vital signs, electrocardiogram (ECG) is widely recognized as a diagnostic tool and standard for medical and research purposes. Longitudinal ECG monitoring shows clear advantages in diagnostic yield [2]. However, the traditional clinical ECG with wet gel electrodes (usually Ag/AgCl electrodes) normally requires a galvanic contact to the body and often skin preparation, which may cause skin irritation and thus poses a large burden for longitudinal monitoring [3]. Dry-electrodes [4]–[5] eliminate the need for gel. However, they still require a direct body contact, which is inconvenient in daily life.

Non-contact capacitively coupled ECG monitoring embedded in beds [6], car seats [7]–[8], or smart clothing [9] can potentially overcome these limitations by providing an easy and unobtrusive ECG measurement without direct contact with skin. To acquire high-quality ECG signals by capacitive electrodes, a variety of solutions ranging from passive electrode design [10]–[12] to the subsequent analog-front-end (AFE) design [13]–[18] have been proposed. Multiple techniques were used for the AFE to enhance the signal quality, such as minimizing common-mode (CM) interference by active shielding [13], carefully designed printed circuit board (PCB) [14], or negative feedback [15]; reducing the noise by adopting a low noise preamplifier [16]; increasing the input impedance by neutralization feedback [17], [18], etc. However, most of these techniques were based on off-the-shelf components thus leading to a system with high complexity and high power consumption. In addition, the major challenges, such as ultra-high input impedance, large common-mode (CM) interferences, and motion artifacts (detailed in Section II) have not been completely addressed in these proposed solutions.

In this work we present an AFE with an ultra-high input impedance up to 400 G Ω (< 0.5 Hz), which can be applied for non-contact capacitively coupled ECG acquisition. The AFE is capable of compensating large CM interferences up to 2.8 V_{PP} and handling 220 mV_{PP} in-band differential artifacts, thus meeting the requirements in the real applications. The AFE

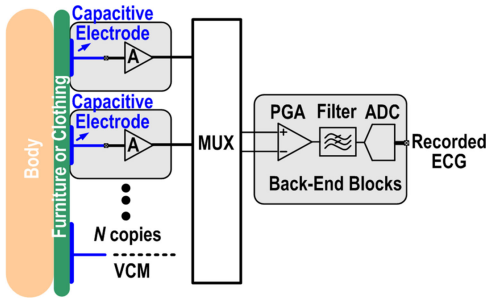


Fig. 1. System architecture of non-contact capacitively coupled ECG acquisition.

compensates the CM interference with an active driven-right-leg (DRL) loop, which boosts the CMRR to 70 dB. Meanwhile, it amplifies the small ECG signals as well as the large differential artifacts with -60 dB total-harmonic-distortion (THD). After digitizing, the differential artifacts can be removed by the back-end digital signal processing and the ECG signals can be extracted.

The paper is organized as follows: in Section II, the main design challenges of the AFE for non-contact capacitively coupled ECG are presented; this is followed by our proposed solutions in Section III (which was first presented in [19]); in Section IV, the measurement results are shown and final conclusions are drawn in Section V.

II. MAIN CHALLENGES

Figure 1 shows the system architecture of the non-contact capacitively coupled ECG acquisition method. One plate of the coupling capacitance is formed by the human body while the other plate is formed by the capacitive electrode which can be integrated into the furniture (e.g., a car seat or a bed) or clothing.

Capacitively coupled ECG signals are amplified by the AFE, which normally drives a connection wire with typically up to 100 pF capacitance. Then, the captured ECG signals are multiplexed to the back-end blocks, consisting of a programmable-gain-amplifier (PGA), a filter and an analog-to-digital converter (ADC). Among the N copies of electrodes, one of them is used for active body reference biasing. The peak-to-peak amplitude of ECG is typically on the order of 1 mV_{PP}. With sufficient amplification, a recording ADC with 7–12 effective-number-of-bits (ENO) would normally suffice to faithfully digitize the ECG signals [20].

A. Ultra-High Input Impedance

Figure 2 shows the typical model of the coupling interface of the non-contact capacitive electrode. The interface, simply modeled by a parallel combination of a coupling capacitance C_S (typically ranging from 10 pF to 200 nF) and a coupling resistance R_S (typically ranging from 1 GΩ to infinity, depending on the material of the interface and whether there exists an air gap), represents a large and varying source impedance (i.e., up to GΩ-range for signals < 10 Hz), requiring a much larger input impedance for the AFE than in a traditional contact-based

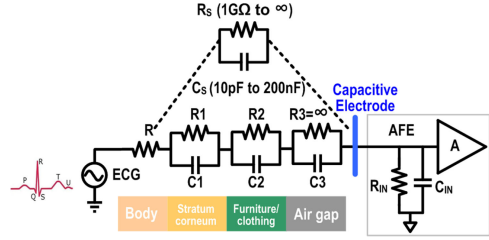


Fig. 2. Typical model of coupling interface.

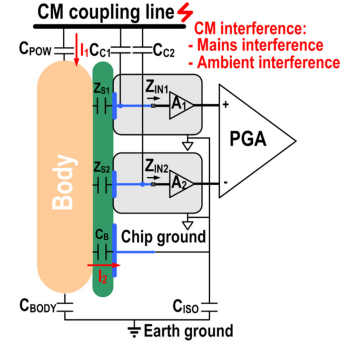


Fig. 3. Coupling mechanisms of the CM interference (CMI).

scenario: at least several GΩ within the ECG bandwidth. In addition, the DC input impedance (R_{IN}) of the AFE inevitably forms a high-pass filter with the coupling capacitance. Assuming C_S is 10 pF, to form a sufficiently low high-pass-frequency (HPF, i.e., < 0.67 Hz for ambulatory ECG monitoring), R_{IN} should be larger than 24 GΩ. Thus the AFE requires an ultra-high input impedance (i.e., $R_{IN} > 100$ GΩ, $C_{IN} < 1$ pF). This is extremely challenging compared to the contact-electrode, which typically requires hundreds of MΩ input impedance.

A chopper amplifier with duty-cycled resistors and auxiliary-path pre-charging was presented in [22], achieving 1.6 GΩ DC input impedance, which is still a bit low for non-contact sensing. A bootstrapped unity-gain buffer achieving 50 TΩ DC input impedance was shown in [13]. However, the unity-gain buffer could not effectively suppress the noise from the subsequent stages. While the overall input-referred noise can also be kept low by inserting a second-stage low-noise amplifier, this will inevitably increase the system power consumption a lot. Moreover, the unity-gain buffer typically drives cables of a certain length between the AFE and the second stage, and hence will be more sensitive to noise pick-up. Therefore, an AFE with sufficient gain is preferable. By introducing pseudo-resistor biasing and self-calibrated positive feedback, 50 GΩ input impedance at 50 Hz was achieved in [18]. However, any leakage current across pseudo-resistors will cause a large input offset voltage whereas the leakage of the input ESD cells may fundamentally limit the DC input impedance.

B. Large Common-Mode (CM) Interference

Due to the ultra-high input impedance, non-contact recording is much more susceptible to CM interference. Fig. 3 shows the coupling mechanisms of the CM interference, which could originate from both mains interference at 50/60 Hz and ambient

interference caused by a moving person or objects nearby. The interference can induce a displacement current (I_1) to the body, a part of which (I_2) can flow to the chip ground and lead to CM variation.

Depending on the coupling capacitance value, the CM interference coupled to the AFE input could be as high as $2 V_{PP}$ (see Appendix A), which tends to saturate the AFE or cause CMRR issues. The mismatch of the high source impedance as well as the gain mismatch of the AFE pair (A1 and A2 in Fig. 3) deteriorate the intrinsic CMRR, which could be inherently limited to around 30 dB [13] and would result in unacceptable high mains interference in any real practical scenario. Therefore, in order to ensure good signal quality, the AFE should be tolerant to at least $2 V_{PP}$ CM interference without saturation. In other words, the CMRR should be at least 70 dB.

Conventionally, the DRL technique improves the CMRR by feeding a CM canceling signal to the subject's body to attenuate the CM interference signal [21]. This technique is very effective in traditional gel-based ECG sensing. However, in the non-contact scenarios, the large and uncontrolled coupling interface impedance makes such a loop difficult to stabilize, especially when the loop gain is quite large [22]. In addition, in the non-contact sensing, since CM interference coupled to the AFE input could be quite large ($> 2 V_{PP}$), the CM -canceling signal must have sufficient swing to effectively compensate the large CM interference.

With feed-forward CM cancellation, [23] presents a neural recording chopper amplifier capable of handling 650 mV_{PP} CM artifacts. The CM feed-forward technique is applied to a non-inverting [24] or an inverting [25] AFE, which boosts the CMRR to 84 dB and 102 dB respectively. These techniques become less effective when the source impedance is high due to the attenuation of the CM feed-forward signal, which is the case in non-contact capacitively coupled scenarios. In addition, they only mitigate the CMRR issues due to the source impedance mismatch, but the die-to-die gain mismatch of the AFE pair could still limit the CMRR.

C. Motion Artifacts

Motion artifacts are one of the major impediments against the acceptance of non-contact measurement in clinical diagnosis. The small coupling capacitance and high relative movement between skin and electrode lead to more artifacts and hence a more challenging AFE design. Longitudinal motion results in variable and imbalanced source impedance, and causes charge accumulation and redistribution. Transverse motion generates friction and induces static electricity on the surface of the coupling capacitor [26].

Differential motion artifacts can be quite large, up to several hundred millivolts in realistic non-contact scenarios [27], [28], which can disturb and potentially saturate the readout channel.

Several approaches have been proposed to address the issue, including: applying digital post-processing with an adaptive filtering [29], computing the estimated motion artifacts based on the electrode-tissue impedance (ETI) measurements in the digital domain and feeding it back to the analog domain [30],

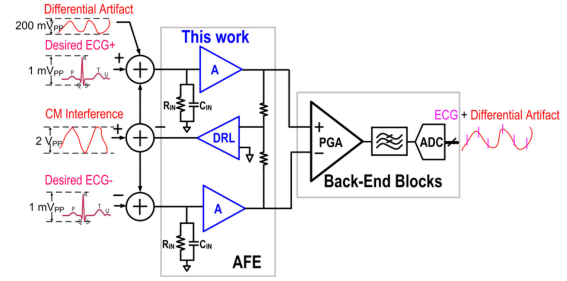


Fig. 4. Block diagrams of the non-contact capacitively coupled ECG acquisition system.

tracking the variation of coupling capacitance, and then injecting the modified information to the output [27]. To enable these back-end signal processing approaches to estimate and remove motion artifacts, the AFE must be tolerant to such large differential artifacts without saturation. Since the artifacts can be up to hundreds of times larger than the ECG signal, the AFE is required to have at least several hundred mV linear-input- range (with 10-bit linearity) in order to ensure a faithful digitizing of the small ECG superimposed on the large motion artifacts.

III. PROPOSED SOLUTIONS

This work presents an AFE with ultra-high input impedance up to $400 \text{ G}\Omega$ ($< 0.5 \text{ Hz}$) which can be applied for non-contact capacitively coupled ECG acquisition. The AFE is capable of handling up to 220 mV_{PP} in-band differential artifacts, compensating up to 2.8 V_{PP} CM interferers with 70 dB CMRR. Although the implementation of the main idea was shown in [19], this paper adds further knowledge and valuable insights in the circuit and system design.

A. System Architecture

Figure 4 shows the block diagrams of the ECG acquisition system. Small ECG signals (1 mV_{PP}) are coupled into the AFE system. Small ECG signals (1 mV_{PP}) are coupled into the AFE along with large CM interference (2 V_{PP}) and differential artifacts (200 mV_{PP}). The AFE compensates the large CM interference with a feedback DRL loop while linearly amplifying the ECG as well as the large differential artifacts. The final digitized ADC output includes both the ECG signal and the differential artifacts. The latter can be subsequently removed by the back-end digital signal processing whereas the former can be extracted.

Figure 5 shows the system architecture of the AFE. In order to improve the signal quality and reduce interference coupling, a single-ended active electrode (AE) – local amplifiers close to the non-contact capacitive electrode plates with active shielding – is adopted [31]. In this way, the length of the critical signal path is minimized thus the interference coupling is reduced. The signal path is shielded by active shielding plates. In contrast to conventional shielding, where the shielding plate is tied to ground, a buffered input which is generated by the AFE biases the shielding plate in active shielding, thus the parasitic capacitance to the input formed by the shielding plate is minimized without significantly reducing the input impedance.

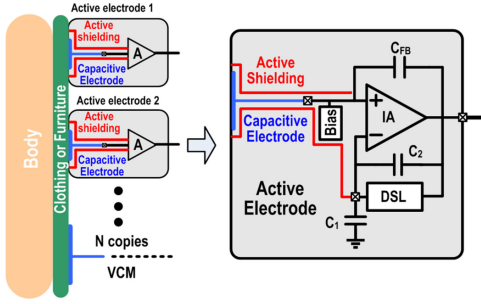


Fig. 5. System architecture of the AFE.

In order to handle large differential artifacts, our solution is to enable the AFE to linearly amplify the ECG signal as well as the artifacts without saturation. The capacitively coupled inverting amplifier (see Fig. 5) is among the most popular topologies used in biopotential signal amplification, which is capable of achieving quite a high linear-input-range [23], [32], [33]. The topology is intrinsically capable of providing ultra-high input impedance with a gain determined by the capacitance ratio ($C_1 + C_2$)/ C_2 . Since the linearity in a feedback system is fundamentally determined by the linearity of the feedback loop, the capacitive feedback with intrinsically high linearity guarantees the large linear-input-range.

The DC-servo loop (DSL) realizes a HPF with a corner higher than the one formed by the input bias. Hence the DSL removes amplifier offset, but also allows amplification while the input is still settling after a large artifact. An extra benefit of the DSL is that the active shielding plate can be driven by the output of the DSL without an additional unity-gain buffer. To prevent saturation due to large artifacts and to increase the DRL swing as well, the AE adopts a ‘moderate’ maximum gain of 20 dB and a ‘high’ supply voltage of 5 V.

B. AE Circuit

Figure 6(a) shows the schematic of the AE. To increase the input impedance, several impedance boosting techniques are introduced. First, the input is biased to VREF via the back-to-back diodes (D_1 and D_2). In normal condition, both diodes are in off-state so that they present ultra-high impedance. In contrast to [18], for a pair of single-ended AEs in this work, the offset introduced by the biasing diodes does not cause saturation thanks to the capacitive coupling. Minimum-sized diodes are adopted to reduce the leakage which may fundamentally limit the DC input impedance. An extra benefit of the biasing scheme is that the non-linear devices quickly recover to a voltage close to VREF after a large input artifact. Fig. 6(c) shows the simulated transient response of the AE when one lead is temporarily disconnected which results in a large disturbance. Compared to the bias scheme with a linear resistor, the proposed non-linear input bias scheme recovers significantly faster from the large disturbance. Secondly, the custom ESD diodes at the inputs are bootstrapped so that their leakage current and parasitic capacitances are minimized without significantly reducing the input impedance. Since the parasitic capacitance of the ESD diode is relatively small compared to the moderate coupling

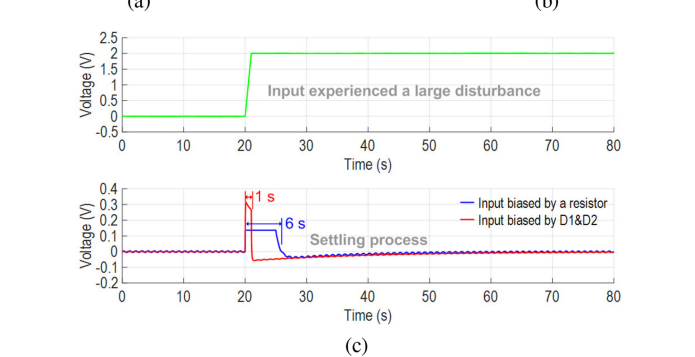
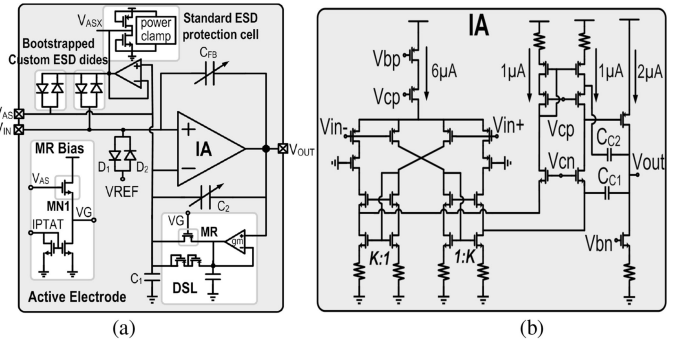


Fig. 6. (a) Schematic of the AE; (b) Schematic of the IA; (c) The simulated transient response with a large disturbance.

capacitance, the noise of the bootstrap buffer is not an issue. A standard ESD protection cell is connected from the bootstrap buffer’s output (node ‘ V_{ASX} ’ in Fig. 6(a)) to the ground. In the layout, the standard ESD protection cell is placed closer to the clamping diodes than the bootstrap buffer. In this way, the ESD events can be discharged rather than damaging the buffer. Finally, a positive feedback capacitor (C_{FB}) is used to compensate and cancel the parasitic input capacitance C_{IN} (including package and PCB parasitic). To avoid overcompensation, the worst case C_{IN} is estimated before setting the value of C_{FB} . Since C_{IN} does not change with time, C_{FB} can be set manually to a constant value. Unfortunately C_{FB} also increases the input referred noise. However, as will be shown later, since the noise is actually dominated by the noise of the input bias network in moderate coupling scenarios, the increased noise due to C_{FB} does not significantly change the total input referred noise.

The input impedance $Z_{IN}(s)$ with the impedance boosting techniques can be expressed by (1):

$$Z_{IN}(s)^{-1} \approx R_{BIAS}^{-1} + [R_{ESD} (1 + A_{BUF})]^{-1} + s [C_{IN} - C_{FB} (A - 1)] \quad (1)$$

where R_{BIAS} and R_{ESD} are the resistance of the input bias diodes and the ESD clamping diodes respectively. R_{ESD} is the equivalent resistance of the ESD devices and models the leakage. A_{BUF} is the gain of the ESD bootstrap buffer, and A is the gain of the AE. A capacitor branch with a compensation range from 0 pF to 6 pF is employed for C_{FB} and the capacitance value is switched according to the different AE gains.

In moderate coupling scenarios, the corner formed by the output pole at the DSL buffer output is higher than the one formed by the input bias. Thus to form a variable HPF, a

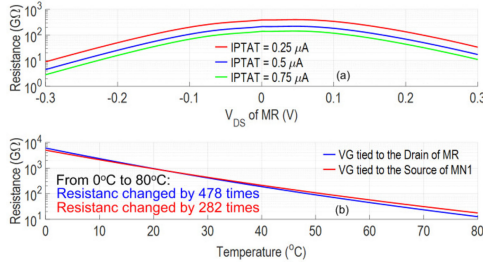


Fig. 7. (a) The simulated resistance value with different bias; (b) The simulated resistance value in the temperature range from 0 °C to 80°C.

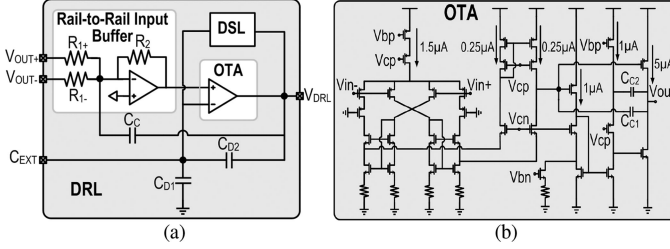


Fig. 8. (a) Schematic of the DRL; (b) Schematic of the OTA.

variable pseudo-resistor (MR) is adopted at the output of the DSL buffer. The ‘drain’ of MR (V_{AS}) is tied to the gate of a native NMOS (MN1), whereas its ‘gate’ (VG) is tied to the ‘source’ of MN1. Since MN1 has a negative threshold voltage, the ‘drain’ voltage of MR can be very close to its ‘gate’ voltage, thus MR presents an ultra-high pseudo-resistance value. The HPF can be programmable by varying the proportional-to-absolute temperature current IPTAT floating into MN1 (in ‘MR Bias’ block). At high temperature, the gate-to-source voltage of MN1 decreases, resulting in a first-order temperature compensation of the pseudo-resistance value. An extra branch of normal pseudo resistor is put in parallel with MR to avoid the potential voltage setup issues. By properly sizing these transistors, MR dominates the resistance at the DSL buffer’s output. Fig. 7(a) shows the simulated resistance value in different bias conditions, tens of GΩ resistance value can be achieved in the range of +/- 0.2 V_{DS} of MR. Thanks to the first-order temperature compensation, the resistance value changes 2 times less in the temperature range from 0 °C to 80°C compared to the one with fixed bias.

Figure 8(b) shows the schematic of the IA. A two-stage cascode compensated IA is used with a recycling folded-cascode first stage [34] and a common-source second stage. Compared to a conventional folded-cascode, the recycling folded-cascode provides K times larger slew rate, where K (= 3) is the current mirror ratio between two input branches. This can be an attractive feature considering the IA will amplify the large swing artifacts, which tends to push the input pair into slew-rate limitation. Source degeneration resistors are added to further reduce the noise as well as to increase the linearity.

C. DRL Circuit

Figure 8(a) shows the schematic of the DRL, which consists of a rail-to-rail input buffer followed by an OTA with capacitive

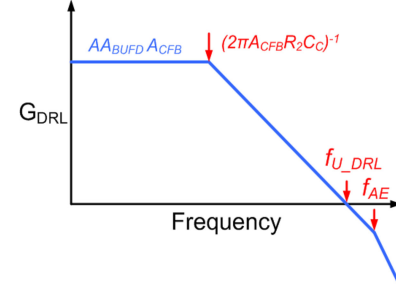


Fig. 9. Magnitude response of the DRL loop gain.

feedback including a DSL. The CM output from the positive and the negative channel (V_{OUT+} and V_{OUT-}) is buffered then amplified by the OTA, where the gain is determined by the capacitance ratio $(C_{D1}+C_{D2})/C_{D2}$. Since the intrinsic CMRR is quite low, typically less than 30 dB, to achieve over 70 dB total CMRR, the DRL loop gain should be at least 40 dB.

To achieve 40 dB DRL loop gain at 60 Hz, the unity-gain-bandwidth of the DRL loop should be at least 6 kHz. The DRL loop stability will be a concern. We can express the frequency domain DRL loop gain $G_{DRL}(s)$ by (2):

$$G_{DRL}(s) \approx A \cdot A_{BUF D} \cdot A_{CFB} \cdot \frac{C_{DRL}}{C_{DRL} + C_{BODY}} \times \frac{1}{1 + \frac{s}{2\pi \cdot f_{AE}}} \cdot \frac{1}{1 + \frac{s}{2\pi \cdot f_{CFB}}} \quad (2)$$

$$f_{AE} \approx \frac{f_{U-IA}}{A} \quad (3)$$

$$f_{CFB} \approx \frac{(f_{U-OTA}^{-1} + 2\pi \cdot R_2 C_C)^{-1}}{A_{CFB}} \quad (4)$$

where A (= 10), $A_{BUF D}$ (= 3.6) and A_{CFB} (= 6) are the gains of the AE, the input buffer and the capacitive feedback OTA respectively. C_{DRL} and C_{BODY} are the DRL coupling capacitance and the body capacitance. f_{AE} and f_{CFB} can be expressed by (3) and (4), where f_{U-IA} and f_{U-OTA} are the unity-gain-bandwidth of the IA and OTA. C_C is the compensation capacitance from the common-mode node to the DRL output. Assume $2\pi \cdot A_{CFB} \cdot R_2 C_C \gg A \cdot f_{IA}^{-1} \gg A_{CFB} \cdot f_{OTA}^{-1}$, Fig. 9 shows the magnitude response of the DRL loop gain and the unity-gain-bandwidth f_{U-DRL} of the DRL loop can be expressed by (5).

$$f_{U-DRL} \approx \frac{A \cdot A_{BUF D}}{2\pi \cdot R_2 C_C} \quad (5)$$

with $R_2 = 2.4 \text{ M}\Omega$ and $C_C = 400 \text{ pF}$, the f_{U-DRL} can be calculated to be 6 kHz, leading to 40 dB loop gain at 60 Hz. To ensure the closed-loop stability, f_{AE} (the first non-dominant pole) should be at least 2.2 times higher than f_{U-DRL} , requiring the -3 dB bandwidth of the AE to be larger than 13.2 kHz.

Apart from the DRL loop, the OTA with capacitance feedback may also pose stability issues when driving huge and variable loading capacitance formed by the DRL plate and the human body (up to several hundreds of pF). Thus the OTA should be sufficiently compensated under the worst case loading capaci-

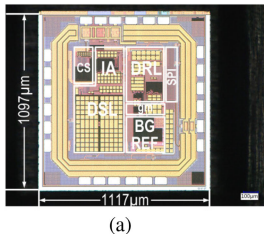


Fig. 10. (a) Micrograph of the fabricated chip; (b) Measured transfer function with C_S ranging from 10 pF to 200 nF.

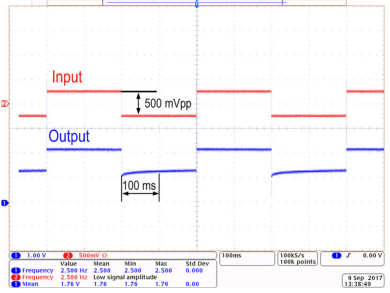


Fig. 11. Measured transient settling behavior.

tance. In addition, the OTA requires high driving capability and slew rate since it is used to amplify and compensate CM interference with large swing and needs to drive a large capacitive load as well. Fig. 8(b) shows the schematic of the three-stage OTA with capacitances feedback compensation [35]. Similar to the IA, the first stage based on the recycling folded-cascode ensures a large slew rate. The class-AB output stage increases its driving capability.

IV. MEASUREMENT RESULTS

The chip including both AE and DRL channel was fabricated in a 0.18 μm CMOS 5V technology. Fig. 10(a) shows the die photograph, occupying an area of 1.23 mm². For a single channel ECG acquisition, 3 chips (a pair for the positive and negative ECG signals, one extra for DRL feedback) are used. Fig. 10(b) shows the measured transfer function of the AE for the whole range of coupling capacitance C_S from 10 pF to 200 nF. Thanks to the ultra-high input impedance, a stable gain of 20 dB is achieved for the whole range. The tunable pseudo-resistance value guarantees HPF < 0.26 Hz in all cases, meeting the requirements of < 0.67 Hz for ambulatory ECG monitoring.

Fig. 11 shows the measured transient settling behavior of the AE. Thanks to the non-linear basing and the DSL schemes, the output settles rapidly within 100 ms with an input step of 500 mV_{PP}.

Figure 12(a) shows the measurement setup of the input impedance. Due to the ultra-high input impedance up to several hundred G Ω , it has been measured indirectly as follows:

1. Place the AE into a Faraday cage (for better shielding from interference) with a resistor R_S (10 G Ω) and AC coupling capacitor C_S (220 nF) in series with its input;
2. Apply an input signal with a known amplitude and then measure the output amplitude from the AE;

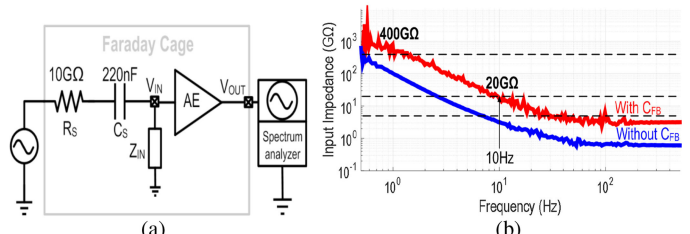


Fig. 12. (a) Measurement setup of the input impedance; (b) Measured input impedance.

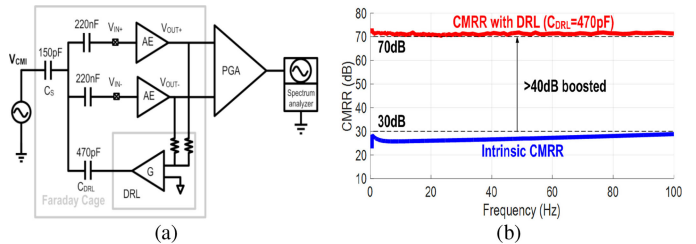


Fig. 13. (a) Demonstration setup of CMRR; (b) Measured intrinsic CMRR and CMRR with DRL.

3. Calculate the AE's input referred amplitude by dividing the output amplitude by the in-band gain;
4. Calculate the input impedance from the voltage division ratio between R_S and Z_{IN} .

Figure 12(b) shows the measured input impedance. The input impedance at 0.5 Hz is boosted by 4 times from 100 G Ω to over 400 G Ω with the positive feedback capacitor C_{FB} . The impedance at 10 Hz is 20 G Ω , corresponding to 0.8 pF input capacitance, which is fundamentally limited by the tuning resolution of C_{FB} . Higher tuning resolution is required to further reduce the input capacitance at 10 Hz.

Figure 13(a) shows the demonstration setup of the CMRR boosting with the proposed DRL. To mimic a realistic CM coupling scenario, an AE pair was put into a Faraday cage with inputs shorted, and the 2.8 V_{PP} CM interference signal (V_{CM1}) was coupled to the inputs via a 150 pF coupling capacitor C_S . The value of C_S is chosen to be 50% higher than the value specified in [36] to give more margin in the non-contact scenarios. The DRL compensation loop is closed via a 470 pF coupling capacitor C_{DRL} (a magnitude close to a real DRL plate) to the CM input. Fig. 13(b) shows the measurement results.

Without an active DRL, the CMRR is indeed limited to <30 dB because of the die-to-die mismatch, but it is boosted by 40 dB to over 70 dB when the DRL is activated. As a result, the AE has a maximum CM-interference-tolerance of 2.8 V_{PP}.

Figure 14(a) shows the measured THD of a single AE. The AE achieves -65/-75 dB HD₃/HD₅ with 40 Hz input signals up to 110 mV_{PP} (220 mV_{PP} for a pair of AEs). Fig. 14(b) shows the measured THD versus the differential input V_{PP} . Over -60 dB THD can be achieved with the differential input amplitude smaller than 220 mV_{PP}, yielding a linear-input-range over 200 mV_{PP}. This is sufficiently high to tolerate the large artifacts that appear in real scenarios. When the input amplitude is large, the THD is fundamentally limited by the non-linearity of the

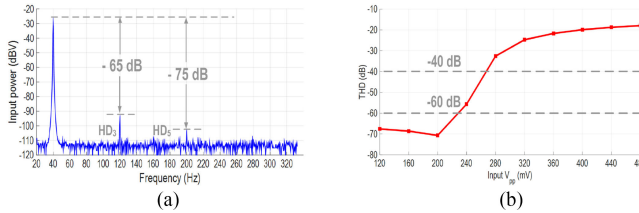


Fig. 14. (a) Measured THD with 110 mV_{PP} input at 40 Hz; (b) Measured THD versus the differential input V_{PP}.

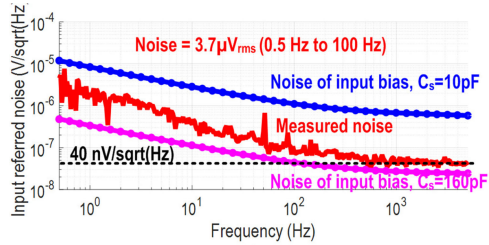


Fig. 15. Measured noise and simulated noise of the input bias.

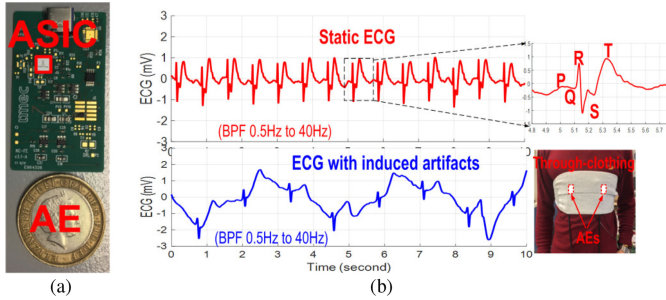


Fig. 16. (a) Photograph of the AE; (b) Real life non-contact capacitively coupled ECG measurement results.

pseudo-resistor (MR). Better THD could be probably achieved by adopting balanced tunable pseudo-resistors structure [37].

The measured noise curve with $C_S = 220 \text{ nF}$ is shown by the red curve in Fig. 15, with a noise floor of $40 \text{ nV}/\sqrt{\text{Hz}}$. The integrated noise from 0.5 Hz to 100 Hz is $3.7 \mu\text{V}_{rms}$, mainly dominated by the flicker noise of the input differential pair. While this seems higher compared to the traditional ECG designs, it is important to understand that the ultra-high input impedance shaped by the C_S contributes to the total system noise. Hence the noise is highly dependent on the value of C_S . In moderate to weakly coupled scenarios ($C_S < 160 \text{ pF}$), the amplifier noise is actually not dominant, as shown by the simulated noise of the input bias in Fig. 15. In addition, the coupling interface can contribute as high as $30 \mu\text{V}_{rms}$ noise and will frequently dominate the electronic noise (see Appendix B). This justifies the reason why we did not burn more current or adopt other techniques such as chopping to further reduce the amplifier's noise.

Figure 16(a) shows the photograph of the AE for the real life non-contact capacitively coupled ECG measurement. Fig. 16(b) shows through-clothing measurement results via two AEs placed on a subject's chest. The upper curve is the static (input-referred) ECG curve, with a typical V3 precordial-leads

shape. Motion is then introduced by moving the body back and forth and the results are shown in the lower curve. Although there is baseband wandering due to the motion, the ECG waves as well as the heart rate are still clearly visible.

Figure 17 shows the on-chair through-clothing (input-referred) ECG measurement results. The AEs are fixed on the seat back, with a DRL plate on the bottom surface of the chair. In such a scenario, although the coupling is relatively weak, the Q-R-S complex is clearly visible in the measurement results, permitting to determine the heart rate and heart rate variability. This is mainly due to the ultra-high input impedance, large linear-input-range, and an active DRL.

Figure 18 shows the measurement results with the ambient CM interference. The interference was introduced on purpose by waving hands nearby the subject. Both the ECG and the DRL output were recorded by an oscilloscope. The DRL output shows a clear variation up to 200 mV due to the ambient CM interference, however, the ECG waveforms are nearly unaffected. This demonstrates the effectiveness of the AE as well as the DRL compensation loop. Table I shows the performance comparison table.

V. CONCLUSIONS

In this paper, we present an AE for non-contact capacitively coupled ECG acquisition. An input impedance boosting by a factor 4 as well as a high-gain (40 dB) active DRL which boosted CMRR to 70 dB enables the capacitive-feedback AE to achieve an ultra-high input impedance of $400 \text{ G}\Omega$ ($< 0.5 \text{ Hz}$), large CM interference tolerance (2.8 V_{PP}), and high linear-input-range (220 mV_{PP}), while presenting acceptable noise performance and consuming less current than the commercial chip. Real life non-contact capacitively coupled ECG acquisition has been demonstrated, obtaining ECG waves and heart rate in the presence of the motion artifacts as well as the ambient interference. The AE provides an alternative fully-integrated, low-cost and low-power solution to the previous systems based on off-the-shelf components [14]–[16], [39], [40].

APPENDIX A

Figure 3 shows the CM interference coupling scheme. For simplicity, we only calculate the magnitude of the CM interference from mains interference at 50 Hz with an amplitude of 220 V_{rms} . With typical values of the coupling capacitance [43] ($C_{POW} = 3 \text{ pF}$, $C_{BODY} = 300 \text{ pF}$, $C_{ISO} = C_B = 600 \text{ pF}$), the calculated displacement current I_1 from the CM coupling line to the body is equal to:

$$I_1(t) = C \frac{dV}{dt} = 3 \text{ pF} \cdot \frac{d[220 \text{ mV} \cdot \sqrt{2} \sin(2\pi \cdot 50 \cdot t)]}{dt}$$

Thus, I_1 has a peak-to-peak value of $0.6 \mu\text{A}_{PP}$. The equivalent chip ground impedance (to the human body) is equal to:

$$Z_B = |s \cdot C_B|^{-1} = |j \cdot 2\pi \cdot 50 \cdot 600 \text{ pF}|^{-1} = 5.3 \text{ M}\Omega$$

Under these capacitance values, half of the displacement current is floating to the chip ground. Thus, the magnitude of the introduced CM interference (the difference between the human

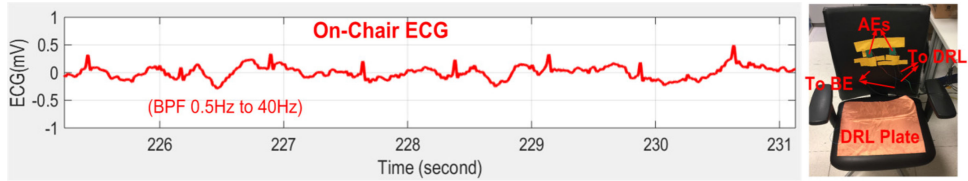


Fig. 17. On-chair though-clothing ECG measurement results. In this weakly coupled scenario, the Q-R-S complex of ECG is clearly visible, permitting to determine heart rate and heart rate variability.

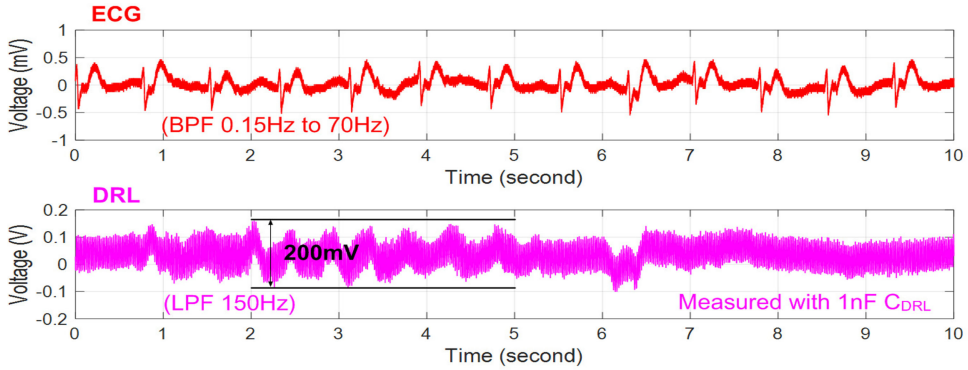


Fig. 18. ECG measurements with environmental CM interference. The DRL output shows a variation up to 200 mV due to the introduced environmental CM interference, however the ECG waveforms in this region are nearly unaffected.

TABLE I
PERFORMANCE COMPARISON TABLE

Parameters	[13] JEMSTC'11	[41] VLSI'16	[23] JSSC'17	[18] JSSC'18	[38] ISSCC'18	[42] Plessey	This work	
Electrode Type	Capacitive	Dry	Capacitive	Capacitive	Capacitive	Capacitive	Capacitive	
Supply (V)	3.3	1.8	1.2	0.8	1.2	4.8-11	5	
Supply current (μA)	4.8	60	2.3	0.32	6.1	2000	AE DRL 18 13	
Midband Gain (dB)	0	0	25.7	34	17.7	34	0/9/13/20	
Input Impedance (GΩ)	@Sub-Hertz	50000 ^[a] @ DC	18@ DC	1.6 @ DC	200@ 1 Hz	1.5@ DC	20 @ DC	400@ 0.5 Hz
	@50Hz	---	6.7	1.6	50	1	---	5.0
Input capacitance (pF)	0.06	~0.2	~1	0.06	~1.6	15	0.8	
CMRR (dB)	---	108	---	66	---	---	>70	
Maximum CM interference tolerance (V _{pp})	---	---	0.65	---	---	---	>2.8	
Linear Input Range (mV _{pp})	---	---	80	<32 ^[b]	200	---	220	
Input referred noise/channel (μV _{rms})	---	0.62 (0.5-100Hz)	1.8 (1-200Hz)	8.26 (1-400Hz)	1.8 (1-200Hz)	---	3.7 (0.5-100Hz)	
With DRL	No	Yes	No	No	No	No	Yes	
Area (mm ²)	---	5.01	0.069	0.58	0.113	---	1.23	
Technology	0.5μm	0.18μm	40nm	0.18μm	40nm	---	0.18μm	

[a] This is the estimated value in [13].

[b] This is the calculated value according to the supply voltage (0.8V) and the voltage gain (34dB).

body to the chip ground) is equal to:

$$V_{CMI} = 0.5 \cdot I_1 \cdot Z_B = 0.5 \cdot 0.6 \mu A_{PP} \cdot 5.3 M\Omega = 1.6 V_{PP}$$

This calculation shows the necessity to make CM interference tolerance > 2V_{PP}.

APPENDIX B

In [44], the author shows by measurement that the R-C thermal noise is accurate at computing the relative noise levels of the

electrode. While the measured noise spectrum does not exactly match thermal noise theory, the model provides a useful starting point and can predict the relative performance of the electrode. In order to make a reasonable estimation of the interface noise, we simulate the integrated noise from 0.5 to 100 Hz with a pair of interface models. The results are shown in Fig. A1. With the capacitance and resistance value sweeping in the design range, the interface noise can be larger than 5 μV_{rms} (in the extreme case even up to 30 μV_{rms}), which will normally dominate the electronic noise.

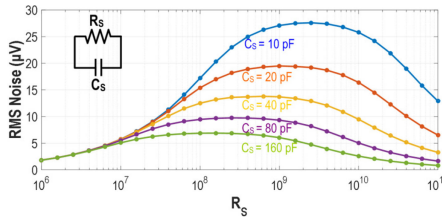


Fig. A1. Simulated interface noise (0.5 Hz to 100 Hz) with the sweeping value of R_s and C_s .

REFERENCES

- [1] World Health Organization, 2016. [Online]. Available: http://www.who.int/cardiovascular_diseases/en/
- [2] A. J. Casson, R. Saunders, and J. C. Batchelor, "Five day attachment ECG electrodes for longitudinal bio-sensing using conformal tattoo substrates," *IEEE Sensors J.*, vol. 17, no. 7, pp. 2205–2214, Apr. 2017.
- [3] N. Meziane, J. G. Webster, M. Attari, and A. J. Nimunkar, "Dry electrodes for electrocardiography," *Physiol. Meas.*, vol. 34, pp. R47–R69, Jul. 2013.
- [4] Y. M. Chi, T. P. Jung, and G. Cauwenberghs, "Dry-contact and noncontact biopotential electrodes: Methodological review," *IEEE Rev. Biomed. Eng.*, vol. 3, pp. 106–119, 2010.
- [5] R. Matthews *et al.*, "Real time workload classification from an ambulatory wireless EEG system using hybrid EEG electrodes," in *Proc. 30th Annu. Int. Conf. IEEE Eng. Med. Biol. Soc.*, Vancouver, BC, Canada, 2008, pp. 5871–5875.
- [6] Y. G. Lim, K. K. Kim, and K. S. Park, "ECG recording on a bed during sleep without direct skin-contact," *IEEE Trans. Biomed. Eng.*, vol. 54, no. 4, pp. 718–725, Apr. 2007.
- [7] T. Matsuda and M. Makikawa, "ECG monitoring of a car driver using capacitively-coupled electrodes," in *Proc. 30th Annu. Int. Conf. IEEE Eng. Med. Biol. Soc.*, Vancouver, BC, Canada, 2008, pp. 1315–1318.
- [8] T. Wartzek, B. Eilebrecht, J. Lem, H. J. Lindner, S. Leonhardt and M. Walter, "ECG on the road: Robust and unobtrusive estimation of heart rate," *IEEE Trans. Biomed. Eng.*, vol. 58, no. 11, pp. 3112–3120, Nov. 2011.
- [9] Y. Sun, X. Yu, J. Berilla, Z. Liu, and G. Wu, "An in-vehicle physiological signal monitoring system for driver fatigue detection," in *Proc. 3rd Int. Conf. Road Saf. Simul.*, Indianapolis, IN, USA, Sep. 2011, pp. 1–16.
- [10] N. Gandhi, C. Khe, D. Chung, Y. M. Chi, and G. Cauwenberghs, "Properties of dry and non-contact electrodes for wearable physiological sensors," in *Proc. Int. Conf. Body Sensor Netw.*, Dallas, TX, USA, 2011, pp. 107–112.
- [11] R. Cardu, P. H. W. Leong, C. T. Jin, and A. McEwan, "Electrode contact impedance sensitivity to variations in geometry," *Physiol. Meas.*, vol. 33, no. 5, pp. 817–830, 2012.
- [12] G. Peng, M. Sterling, and M. Bocko, "Non-contact, capacitive biosensor electrodes for electrostatic charge reduction," in *Proc. IEEE Sensors*, Baltimore, MD, USA, 2013, pp. 1–4.
- [13] Y. M. Chi, C. Maier, and G. Cauwenberghs, "Ultra-high input impedance, low noise integrated amplifier for noncontact biopotential sensing," *IEEE J. Emerg. Sel. Topics Circuits Syst.*, vol. 1, no. 4, pp. 526–535, Dec. 2011.
- [14] T. J. Sullivan, S. R. Deiss and G. Cauwenberghs, "A low-noise, non-contact EEG/ECG sensor," in *Proc. IEEE Biomed. Circuits Syst. Conf.*, Montreal, QC, Canada, 2007, pp. 154–157.
- [15] H.-C. Lee *et al.*, "An ECG front-end subsystem for portable physiological monitoring applications," in *Proc. Int. Conf. Elect. Inf. Control Eng.*, Wuhan, China, 2011, pp. 6359–6362.
- [16] G. Peng and M. F. Bocko, "A low noise, non-contact capacitive cardiac sensor," in *Proc. Annu. Int. Conf. IEEE Eng. Med. Biol. Soc.*, San Diego, CA, USA, 2012, pp. 4994–4997.
- [17] S. Joshi, C. Kim, and G. Cauwenberghs, "A $6\mu\text{W}/\text{MHz}$ charge buffer with 7fF input capacitance in 65 nm CMOS for non-contact electropotential sensing," in *Proc. IEEE Int. Symp. Circuits Syst.*, Montreal, QC, Canada, 2016, pp. 2907–2907.
- [18] J. Lee, G. H. Lee, H. Kim, and S. Cho, "An ultra-high input impedance analog front end using self-calibrated positive feedback," *IEEE J. Solid-State Circuits*, vol. 53, no. 8, pp. 2252–2262, Aug. 2018.
- [19] M. Chen *et al.*, "A $400\text{ G}\Omega$ input-impedance, 220 mV_{pp} linear-input-range, 2.8V_{pp} CM-interference-tolerant active electrode for non-contact capacitively coupled ECG acquisition," in *Proc. IEEE Symp. VLSI Circuits*, Honolulu, HI, USA, Jun. 2018, pp. 129–130.
- [20] M. Mollazadeh, K. Murari, G. Cauwenberghs, and N. Thakor, "Micropower CMOS integrated low-noise amplification, filtering, and digitization of multimodal neuropotentials," *IEEE Trans. Biomed. Circuits Syst.*, vol. 3, no. 1, pp. 1–10, Feb. 2009.
- [21] B. B. Winter and J. G. Webster, "Driven-right-leg circuit design," *IEEE Trans. Biomed. Eng.*, vol. BME-30, no. 1, pp. 62–66, Jan. 1983.
- [22] *Improving Common-Mode Rejection Using the Right-Leg Drive Amplifier*, Texas Instrum., Dallas, TX, USA, 2011. [Online]. Available: <http://www.ti.com/general/docs>
- [23] H. Chandrakumar and D. Marković, "An 80-mVpp linear-input range, $1.6\text{-G}\Omega$ input impedance, low-power chopper amplifier for closed-loop neural recording that is tolerant to 650-mVpp common-mode interference," *IEEE J. Solid-State Circuits*, vol. 52, no. 11, pp. 2811–2828, Nov. 2017.
- [24] J. Xu *et al.*, "A wearable 8-channel active-electrode EEG/ETI acquisition system for body area networks," *IEEE J. Solid-State Circuits*, vol. 49, no. 9, pp. 2005–2016, Sep. 2014.
- [25] J. Xu, B. Büsze, C. van Hoof, K. A. A. Makinwa, and R. F. Yazicioglu, "A 15-channel digital active electrode system for multi-parameter biopotential measurement," *IEEE J. Solid-State Circuits*, vol. 50, no. 9, pp. 2090–2100, Sep. 2015.
- [26] Y. Sun and X. B. Yu, "Capacitive biopotential measurement for electrophysiological signal acquisition: A review," *IEEE Sensors J.*, vol. 16, no. 9, pp. 2832–2853, May 2016.
- [27] A. Serteyn, R. Vullings, M. Meftah, and J. W. M. Bergmans, "Motion artifacts in capacitive ECG measurements: Reducing the combined effect of dc voltages and capacitance changes using an injection signal," *IEEE Trans. Biomed. Eng.*, vol. 62, no. 1, pp. 264–273, Jan. 2015.
- [28] H. Antink C, F. Schulz, S. Leonhardt, and M. Walter, "Motion artifact quantification and sensor fusion for unobtrusive health monitoring," *Sensors*, vol. 18, 2018, Art. no. 38.
- [29] "Low-power, 2-channel, 24-bit analog front-end for biopotential measurements," Texas Instrum., Dallas, TX, USA, 2012. [Online]. Available: <http://www.ti.com/lit/ds/sbas502b/sbas502b.pdf>
- [30] N. van Helleputte *et al.*, "A $345\ \mu\text{W}$ multi-sensor biomedical SoC with bio-impedance, 3-channel ECG, motion artifact reduction, and integrated DSP," *IEEE J. Solid-State Circuits*, vol. 50, no. 1, pp. 230–244, Jan. 2015.
- [31] R. J. Prance, T. D. Clark, H. Prance, and A. Clippingdale, "Noncontact VLSI imaging using a scanning electric potential microscope," *Meas. Sci. Technol.*, vol. 8, pp. 1229–1235, Aug. 1998.
- [32] R. R. Harrison and C. Charles, "A low-power low-noise CMOS amplifier for neural recording applications," *IEEE J. Solid-State Circuits*, vol. 38, no. 6, pp. 958–965, Jun. 2003.
- [33] V. Majidzadeh, A. Schmid, and Y. Leblebici, "Energy efficient low-noise neural recording amplifier with enhanced noise efficiency factor," *IEEE Trans. Biomed. Circuits Syst.*, vol. 5, no. 3, pp. 262–271, Jun. 2011.
- [34] R. S. Assaad and J. Silva-Martinez, "The recycling folded cascode: A general enhancement of the folded cascode amplifier," *IEEE J. Solid-State Circuits*, vol. 44, no. 9, pp. 2535–2542, Sep. 2009.
- [35] X. Peng and W. Sansen, "Transconductance with capacitances feedback compensation for multistage amplifiers," *IEEE J. Solid-State Circuits*, vol. 40, no. 7, pp. 1514–1520, Jul. 2005.
- [36] *Medical Electrical Equipment—Part 2-47*, IEC Standard 60601-2-47, 2012.
- [37] X. Zou, X. Xu, L. Yao, and Y. Lian, "A 1-V 450-nW fully integrated programmable biomedical sensor interface chip," *IEEE J. Solid-State Circuits*, vol. 44, no. 4, pp. 1067–1077, Apr. 2009.
- [38] H. Chandrakumar and D. Markovic, "A 15.2-enob continuous-time $\Delta\Sigma$ ADC for a $7.3\ \mu\text{W}$ 200mVpp -linear-input-range neural recording front-end," in *Proc. IEEE Int. Solid State Circuits Conf.*, San Francisco, CA, USA, 2018, pp. 232–234.
- [39] T. Torfs, Y. H. Chen, H. Kim, and R. F. Yazicioglu, "Noncontact ECG recording system with real time capacitance measurement for motion artifact reduction," *IEEE Trans. Biomed. Circuit Syst.*, vol. 8, no. 5, pp. 617–625, Oct. 2014.
- [40] I. D. Castro, R. Morariu, T. Torfs, C. van Hoof, and R. Puers, "Robust wireless capacitive ECG system with adaptive signal quality and motion artifact reduction," in *Proc. IEEE Int. Symp. Med. Meas. Appl.*, Benevento, Italy, 2016, pp. 1–6.
- [41] X. Zhou, Q. Li, S. Kilsgaard, F. Moradi, S. L. Kappel, and P. Kidmose, "A wearable ear-EEG recording system based on dry-contact active electrodes," in *Proc. IEEE Symp. VLSI Circuits*, Honolulu, HI, USA, 2016, pp. 1–2.
- [42] *PS25451 Datasheet*, Plessey, Ilford, U.K., 2018. [Online]. Available: <http://www.plessey.com/documents/PS25451.pdf>

- [43] A. C. Metting van Rijn, A. Peper, and C. A. Grimbergen, "High-quality recording of bioelectric events," *Med. Biol. Eng. Comput.*, vol. 28, no. 5, pp. 389–397, Sep. 1990.
- [44] Y. M. Chi, "Non-contact biopotential sensing," Ph.D. dissertation, Dept. Elect. Eng., Univ. California, San Diego, CA, USA, 2011.



Tom Torfs received the graduate degree in electronics engineering from KIH De Nayer, Sint-Katelijne-Waver, Belgium, in 2001, and the master's degree in engineering—biomedical technology—from KU Leuven, Leuven, Belgium, in 2010. Since 2001, he has been with IMEC, Heverlee, Belgium, as a Systems Researcher, and an Architect and Principal Engineer, designing systems-based around IMEC circuit, sensor and packaging technologies, with a focus on sensors for biomedical applications. He has coauthored more than 80 publications, 12 as lead author

and has four patents to his credit.



Mingyi Chen (M'16) received the B.S. and M.S. degrees from Tianjin University, Tianjin, China, in 2004 and 2007, respectively, and the Ph.D. degree from the Chinese Academy of Science, Beijing, China, in 2014, all in microelectronics and solid-state electronics.

From 2007 to 2009, he was an IC Design Engineer with Trident Multimedia Technology Inc., working on mixed-signal circuits for HDTV chips. From 2009 to 2015, he was a Senior Analog/RF IC Designer with Smart-Chip Integration Inc., working on wireless communication chips. In 2015, he joined Shanghai Jiao Tong University (SJTU), Shanghai, China, as a Postdoctoral Researcher with the Biomedical Circuit and System Laboratory. From 2016 to 2018, he was a Postdoctoral Research Fellow with the MEDIC team, IMEC, Leuven, Belgium. He is currently a tenure track Assistant Professor with SJTU. His research interests include bioelectronic circuits and systems, ultra-low power wireless and energy harvesting for IoT, and high-speed and high-resolution data converters.



Qiuyang Lin (S'16) received the B.S. degree in electrical engineering from the Dalian University of Technology, Dalian, China, in 2014, and the M.S. degree in electrical engineering from the Delft University of Technology, Delft, The Netherlands, in 2016. In 2016, he moved to IMEC Leuven, Leuven, Belgium, and the University of Leuven, Leuven, Belgium, where he is currently working toward the Ph.D. degree in biomedical integrated circuit design. His research interest includes biomedical readout circuits, ADC, low noise, mix-signal circuits and system for optical sensor, sensor interface, and wearable biomedical applications.



Chris van Hoof (M'91) received the Ph.D. degree in electrical engineering from the University of Leuven, Leuven, Belgium, in 1992. He is a Senior Director of Connected Health Solution, IMEC, Leuven, Belgium, and also IMEC Fellow. He is also a Full Professor with the University of Leuven. He has a track record of more than 25 years of initiating, executing, and leading national and international contract R&D with imec. His work resulted in five startups (four in the healthcare domain). He has authored or coauthored more than 700 papers in journals and conference proceedings and given more than 100 invited talks. His research covered highly diverse technical fields, such as sensors and imagers, MEMS and autonomous microsystems, wireless sensors, body-area networks, patient monitoring solutions, and digital phenotyping.



Ho Sung Chun (M'13) received the B.E. degree in electrical engineering from the University of Sydney, Camperdown, NSW, Australia, in 2005, and the Ph.D. degree in electrical engineering from the University of New South Wales, Sydney, NSW, Australia, in 2012. In 2011, he joined to Bionic Vision Australia, Melbourne, VIC, Australia, as a researcher, working on Bionic Eye project. From 2014 to 2015, he was a senior Analog Design Consultant with Australian Semiconductor Technology Company, Adelaide, SA, Australia. Since 2015, he has been an Analog Design Engineer with IMEC, Heverlee, Belgium, mainly for biomedical applications.



Guoxing Wang (M'06–SM'13) received the Ph.D. degree in electrical engineering from the University of California at Santa Cruz, Santa Cruz, CA, USA, in 2006.

He was a member of the Technical Staff with Agere Systems, San Jose, CA, USA, from 2006 to 2007. From 2007–2009, he joined the Second Sight Medical Products, Sylmar California, where he designed the integrated circuits chip that went into the eyes of blind people to restore vision. Currently, he is an Associate Professor with the School of Microelectronics, Shanghai Jiao Tong University, Shanghai, China. He has authored or coauthored in various peer-reviewed journals and conferences. His current research interests include biomedical electronics, and bio-inspired circuits and systems. He was the Technical Program Chair for the IEEE Conference on Biomedical Circuits and Systems in 2016. He was the local Chair for the first IEEE Green Circuits and Systems and the second Asia Pacific Conference on Postgraduate Research in Microelectronics & Electronics (PrimeAsia), both in 2010. He is a member of the IEEE Biomedical Circuits and Systems Technical Committee. He is currently the Deputy Editor-in-Chief for the IEEE TRANSACTIONS ON BIOMEDICAL CIRCUITS AND SYSTEMS from 2016 to 2019 and the Vice President of the IEEE Circuits and Systems Society from 2019 to 2020. He was an Associate Editor for the IEEE TRANSACTIONS ON CIRCUITS AND SYSTEMS II, from 2012 to 2015, and a Guest Editor for the IEEE JOURNAL ON EMERGING AND SELECTED TOPICS IN CIRCUITS AND SYSTEMS and the IEEE TRANSACTIONS ON BIOMEDICAL CIRCUITS AND SYSTEMS, both in 2014.



Iván Dario Castro received the degree in biomedical engineering from the Universidad Autónoma de Occidente, Cali, Colombia, in 2011, and the joint M.Sc. degree in biomedical engineering with emphasis in biomedical instrumentation from Ghent University, Ghent, Belgium, and from Czech Technical University, Prague, Czech Republic, in 2014. He is currently working toward the Ph.D. degree in engineering science with the Department of Electrical Engineering, KU Leuven, Leuven, Belgium, and the Connected Health Solutions Group, R&D Institute IMEC, Leuven, Belgium. His research interests include unobtrusive acquisition of biomedical signals, biomedical signal processing, and digital health solutions.



Yong Lian (M'90–SM'99–F'09) research interests include biomedical circuits and systems, and signal processing. He is the President of the IEEE Circuits and Systems (CAS) Society, the Chair of the IEEE Periodicals Partnership Opportunities Committee, and a member of the IEEE Periodicals Committee, the IEEE Biomedical Engineering Award Committee, and Steering Committee of the IEEE TRANSACTIONS ON BIOMEDICAL CIRCUITS AND SYSTEMS. He is the founder of the IEEE Biomedical Circuits and Systems Conference and the Asia Pacific Conference on Postgraduate Research in Microelectronics and Electronics (PrimeAsia). He was the Vice-President for publications and the Vice-President for Region 10 of the IEEE CAS Society, and many other roles in IEEE. He was the Editor-in-Chief for the IEEE TRANSACTIONS ON CIRCUITS AND SYSTEMS Part II for two terms. He was the recipient of more than 15 awards for his research including IEEE Circuits and Systems Society's Guillemin-Cauer Award, IEEE Communications Society Multimedia Communications Best Paper Award, Institution of Engineers Singapore Prestigious Engineering Achievement Award, and Winner of the Design Contest Award in ISLPED2015. He is a Fellow of the Academy of Engineering Singapore.



Nick van Helleputte (M'07) received the M.S. degree in electrical engineering from Katholieke Universiteit Leuven, Leuven, Belgium, in 2004, and the Ph.D. degree from MICAS Research Group, Katholieke Universiteit Leuven, in 2009. His Ph.D. research focused on low-power ultra-wide-band analog front-end receivers for ranging applications. He joined IMEC, Heverlee, Belgium, in 2009, as an Analog R&D Design Engineer. He is currently the Team Leader of the Biomedical Circuits and Systems Team. He has been involved in analog and mixed-signal ASIC design for wearable and implantable healthcare applications. His research focus is on ultra-low-power circuits for biomedical applications. He is an SSCS member and served on the technical program committee of VLSI circuit's symposium and ISSCC.